

# Surface wave phase-velocity tomography based on multichannel cross-correlation

Ge Jin and James B. Gaherty

Lamont-Doherty Earth Observatory, Columbia University New York, NY, USA. E-mail: [ge.jin@ldeo.columbia.edu](mailto:ge.jin@ldeo.columbia.edu)

Accepted 2015 February 16. Received 2015 February 1; in original form 2014 May 30

## SUMMARY

We have developed a new method to retrieve seismic surface wave phase velocity using dense seismic arrays. The method measures phase variations between nearby stations based on waveform cross-correlation. The coherence in waveforms between adjacent stations results in highly precise relative phase estimates. Frequency-dependent phase variations are then inverted for spatial variations in apparent phase velocity via the Eikonal equation. Frequency-dependent surface wave amplitudes measured on individual stations are used to correct the apparent phase velocity to account for multipathing via the Helmholtz equation. By using coherence and other data selection criteria, we construct an automated system that retrieves structural phase-velocity maps directly from raw seismic waveforms for individual earthquakes without human intervention. The system is applied to broad-band seismic data from over 800 events recorded on EarthScope's USArray from 2006 to 2014, systematically building up Rayleigh-wave phase-velocity maps between the periods of 20 and 100 s for the entire continental United States. At the highest frequencies, the resulting maps are highly correlated with phase-velocity maps derived from ambient noise tomography. At all frequencies, we observe a significant contrast in Rayleigh-wave phase velocity between the tectonically active western US and the stable eastern US, with the phase velocity variations in the western US being 1–2 times greater. The Love wave phase-velocity maps are also calculated. We find that overtone contamination may produce systemic bias for the Love-wave phase-velocity measurements.

**Key words:** Broad-band seismometers; Surface waves and free oscillations; Seismic tomography; Wave propagation; Dynamics of lithosphere and mantle; North America.

## 1 INTRODUCTION

Seismic surface waves represent one of the primary means for scientists to probe the structure of Earth's crust and upper mantle. Surface waves provide direct constraints on both absolute velocity and relative velocity variations, and analysis of waves with different periods provides sensitivity to different depths. These velocity variations in turn provide some of the best available constraints on a variety of geodynamic parameters, including absolute and relative variations in temperature, crust and mantle composition, the presence or absence of fluid (melt) phases, and the distribution and orientation of flow-induced mineral fabric. In many cases, however, resolution of these properties is limited by uncertainties in observed surface wave velocities due to complexity in the seismic wavefield. Because they sample the highly heterogeneous outer shell of the Earth, surface waves often contain waveform complexity (Fig. 1) caused by focusing and defocusing effects (often termed scattering or multipathing) that makes measurement of wave velocity uncertain.

In recent years, a number of investigators have developed data-analysis schemes designed to more robustly estimate surface wave velocities in the presence of multipathing (e.g. Friederich & Wielandt 1995; Forsyth & Li 2005; Yang & Forsyth 2006; Lin *et al.*

2009; Pollitz & Snoke 2010; Lin & Ritzwoller 2011; Yang *et al.* 2011). These techniques exploit arrays of seismic stations to better quantify the detailed character of the surface wavefield, specifically by combining measurements of both phase and amplitude between stations. These observations can be modelled in the context of wavefield character, for example local plane-wave propagation direction (e.g. Forsyth & Li 2005) or apparent velocities (Lin *et al.* 2009), as well as the structural phase velocity associated with the underlying media. The techniques are particularly useful for estimating structural velocities in localized regions spanning a receiver array, as opposed to along the entire path from the source to the receiver employed in global (e.g. Levshin *et al.* 1992; Li & Romanowicz 1996; Ekström *et al.* 1997) and some regional (e.g. Chen *et al.* 2007; Tape *et al.* 2010; Zhu *et al.* 2012) analyses. The estimates of structural phase or group velocities across the array can then be inverted for models of seismic velocity through the crust and mantle beneath the array, with greater confidence and accuracy than when using phase information alone (e.g. Pollitz & Snoke 2010; Lin & Ritzwoller 2011; Rau & Forsyth 2011; Yang *et al.* 2011). Among the studies, Lin & Ritzwoller (2011) first demonstrate the feasibility of using the Helmholtz equation to improve the accuracy of surface wave phase velocity measurements using a dense array.

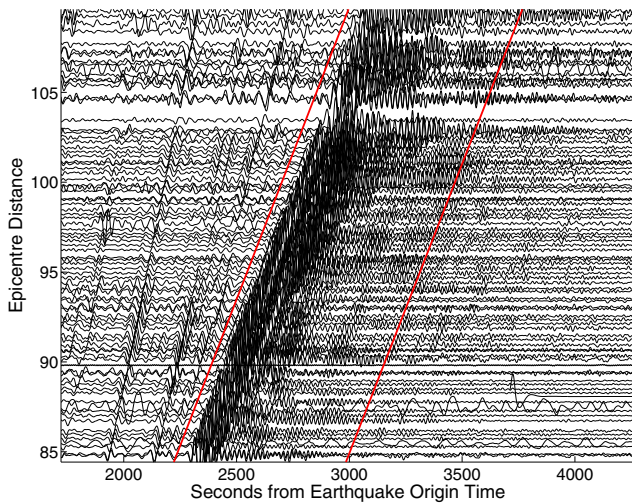


**Figure 1.** USAArray vertical component records for the 2009 January 18, earthquake near Kermadec Islands, New Zealand ( $M_w = 6.4$ ). Red lines show the autoselected window function  $W_S$  to isolate the fundamental Rayleigh wave energy. The variations of the coda length and amplitude indicate the scattering effect caused by lateral heterogeneities.

One of the challenges of the array-based approaches is to efficiently process large data sets that are now available in many regions, with the EarthScope USAArray transportable array (TA) representing an excellent example. Between 2004 and 2014 March, USAArray occupied more than 2700 locations with broad-band seismic stations that were operated for at least 18 months, and recorded more than 800 shallow earthquakes with magnitude 6 or larger. This large data set is ideal for surface wave analysis. Several studies have published surface wave results based on a subset of this database (e.g. Yang & Ritzwoller 2008; Pollitz & Snook 2010; Lin & Ritzwoller 2011; Rau & Forsyth 2011; Bailey *et al.* 2012; Foster *et al.* 2014a). The communication system installed at the sites allows for real-time data collection and archiving. Such a growing data set requires an automated system to accommodate the speed of data growth.

We have developed a new algorithm to accurately and automatically estimate structural phase velocities from broad-band recordings of surface waves propagating across an array of receivers. The analysis is based on the notion that waveform cross-correlation provides a highly precise and robust quantification of relative phase between two observed waveforms, if the waveforms are similar in character. This notion is routinely exploited in body-wave analyses for structure (e.g. VanDecar & Crosson 1990) and source (e.g. Schaff & Beroza 2004) characteristics.

In surface wave analysis, the application of cross-correlation (e.g. Landisman *et al.* 1969) has been mainly applied between two stations on or close to the same great circle with the earthquake (e.g. Knopoff *et al.* 1966; Brisbourne & Stuart 1998; Yao *et al.* 2005). This restriction significantly limits the number of usable measurements, and assuming great-circle propagation can lead to systemic bias in the presence of multipathing and other realistic wave-propagation effects (e.g. Foster *et al.* 2014a). We avoid these limitations by applying a multichannel approach, measuring frequency-dependent phase delays between all possible nearby station pairs, without assuming surface wave propagation following the great-circle path. The measured phase delays form a ideal data set that can be modelled to retrieve both phase velocities and propagation directions via the Eikonal equation (Lin *et al.* 2009).

We build our cross-correlation technique upon the generalized seismological data functional (GSDF) analysis of Gee & Jordan (1992), which utilizes cross-correlation between observed and synthetic seismograms to quantify phase and amplitude behaviour of any general seismic waveform, including surface waves (e.g. Gaherty *et al.* 1996). By applying this quantification to cross-correlation functions between surface waves observed at two nearby stations, we generate highly robust and precise estimates of relative phase delay times between the stations, due to the similar nature of the recorded waveforms. The procedure is applicable to arrays across a variety of scales, from the continental scale of EarthScope's TA, to the few 100s km spanned by a typical PASSCAL experiment, to 100s of metres in industry experiments, and is amenable to automated analyses with minimal analyst interaction. The resulting delay times and associated amplitudes can be modelled in the context of both wave-propagation directions and structural velocities via the Helmholtz equation. Here, we outline the analysis, demonstrate the automated data processing while applying it on the USAArray data (including a brief discussion of the continental-scale phase velocity results), and discuss its comparison to the existing methods. The automated procedure we described here is adopted by IRIS as a data product to provide weekly updated phase-velocity maps of US continent (<http://www.iris.edu/ds/products/aswms/>).

## 2 METHODOLOGY

### 2.1 Interstation phase delays

The methodology is based on the GSDF work flow presented by Gee & Jordan (1992), and subsequently utilized for regional upper mantle and crustal modelling (e.g. Gaherty & Jordan 1995; Gaherty *et al.* 1996; Gaherty 2001, 2004; Chen *et al.* 2007; Gaherty & Dunn 2007). In those analyses, the starting point consists of an observed broad-band seismogram containing all seismic phases of interest, and a complete synthetic seismogram relative to which the phase delays and amplitude anomalies can be measured. Here, we substitute a seismogram from a nearby station for the synthetic waveform, and measure phase and amplitude differences between phases of interest recorded at the two stations. Waveforms from these two stations are presented as  $S_1$  and  $S_2$  here (Fig. 2). Because this is the first application of GSDF to a multichannel analysis, we summarize the steps in some detail. Gee & Jordan (1992) provides a full theoretical presentation of GSDF.

The first step is to isolate the signal of interest in the time domain. In the USAArray application, we applied a window function  $W_S$  that includes the primary surface wave (Rayleigh on vertical-component record, and Love on the transverse component) and most of its coda. Including the coda is useful, in that it is often highly correlated at stations within 1–2 wavelengths, as shown in Fig. 2. We then calculate the cross-correlation function  $C(t)$  (cross-correlogram) between  $S_1$  and  $W_S S_2$ , defined as:

$$C(t) = S_1 \star W_S S_2, \quad (1)$$

$C(t)$  contains the delay or lag information of all coherent signals, with the peak corresponding roughly to a wide-band group delay between the two stations, with a centre frequency defined by the dominant energy in the data, typically around the period of 30 s for teleseismic Rayleigh waves. We further isolate the dominant energy in the cross-correlation function in the time domain by applying a window function  $W_c$  around the peak of the cross-correlation

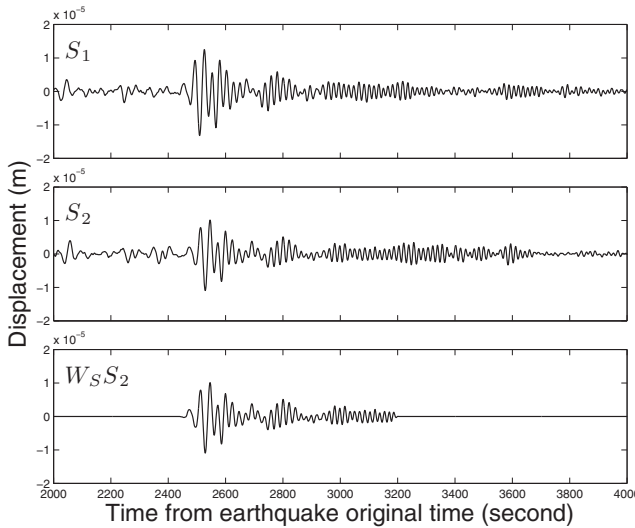


**Figure 2.** Sample waveforms from a nearby station pair for the Kermadec Islands earthquake shown in Fig. 1. Record  $S_1$  is from the station W17A, and record  $S_2$  is from the station W18A. The two stations are 89 km apart. The third panel demonstrates the effect of window function  $W_S$  to isolate the energy of fundamental Rayleigh waves.

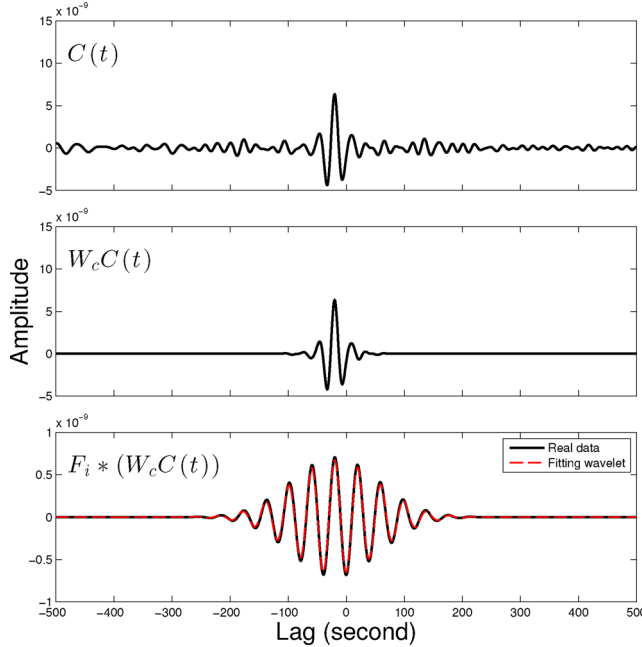


**Figure 3.** The cross-correlation procedures for the station pair shown in Fig. 2. Top: the original cross-correlogram. Middle: the windowed cross-correlogram. Bottom: the narrow-band filtered cross-correlogram (40 s) with the five-parameter wavelet.

function, producing  $W_c C(t)$ . The window function we apply here has a total length of 300 s with 75 s Hanning taper at both ends.

We then isolate the signals of interest in the frequency domain by convolving a sequence of Gaussian, narrow-band filters with  $W_c C(t)$ , forming a set of filtered correlograms  $F_i(\omega_i)^* W_c C(t)$ , where  $F_i(\omega_i)$  corresponds to each filter at centre frequency  $\omega_i$  (Fig. 3). These filtered correlograms provide information of the frequency-dependent group and phase delays between the two stations, as well as the coherence between the two signals. The frequency-dependent delays provide the fundamental data for determining the phase-velocity characteristics of the wavefield and the structure

being sampled. In the application presented here, we are interested in characterizing the phase velocity of fundamental-mode surface waves in the 20–100 s period band, and so we apply a sequence of eight narrow-band, zero-phase Gaussian filters with a bandwidth of approximately 10 per cent of the centre frequency.

The narrow-band filtered cross-correlation function can be well approximated by a five-parameter wavelet which is the product of a Gaussian envelope and a cosine function:

$$F_i * W_c C(t) \approx A G_a[\sigma(t - t_g)] \cos[\omega(t - t_p)] \quad (2)$$

(Gee & Jordan 1992). In this equation,  $t_g$  and  $t_p$  represent the frequency-dependent group and phase delays between the two stations, respectively,  $G_a$  is the Gaussian function,  $A$  is a positive scale factor,  $\sigma$  is the half-bandwidth and  $\omega$  is the centre frequency of the narrow-band waveform. These parameters are obtained by minimizing the misfit between the predicted wavelet and the observed narrow-band cross-correlogram using a non-linear least-squares inversion.

The raw phase delays are then checked and corrected for cycle-skipping. This is a particular important problem for the higher frequency observations, and/or for station pairs with relatively large separation, for which the phase delay between the two stations may approach or exceed the period of the observation, and the choice of cycle can be ambiguous. This problem is naturally avoided by only estimating the phase delays between relatively close station pairs. In the USAarray application, we only measure station pairs within 200 km, which is less than three wavelengths of the shortest period (20 s). As a result, a very rough estimation of reference phase velocity allows for unambiguous selection of the correct phase delay.

The window function  $W_S$  may also introduce bias in the measurement, simply by altering the input seismograms at the edges of the window. To account for this, we calculate the cross-correlation between  $S_2$  and the isolation filter,  $W_S S_2$ .

$$\tilde{C}(t) = S_2 * W_S S_2, \quad (3)$$

$$F_i * W_c \tilde{C}(t) \approx \tilde{A} G_a[\tilde{\sigma}(t - \tilde{t}_g)] \cos[\tilde{\omega}(t - \tilde{t}_p)]. \quad (4)$$

Since  $S_2$  and  $W_S S_2$  are similar within the window of interest,  $\tilde{C}(t)$  is similar to the autocorrelation function of  $W_S S_2$  with the group delay and phase delay close to zero. Any non-zero phase change corresponds to a delay associated with the windowing process, and by assuming that this windowing delay will be similar for the cross-correlation  $C(t)$ , we calculate a final set of bias-corrected delay times

$$\delta\tau_p = t_p - \tilde{t}_p, \quad (5)$$

$$\delta\tau_g = t_g - \tilde{t}_g. \quad (6)$$

As pointed out by Gee & Jordan (1992), the windowing function  $W_c$  around the peak of the wide-band cross-correlation function may also introduce a bias in the frequency-dependent phase delays. This bias is caused by the centre of the window function not coinciding with the actual group delay at each frequency. In this application this bias is generally negligible, since the cross-correlation measurements are only taken between nearby stations, and plus the dispersion in group delay is small.

We perform this phase-delay estimation between a given station and several nearby stations, generally those within 200 km. Fig. 4 displays the raw phase delays for a representative event recorded across the transportable array. The observed variations are controlled primarily by structural variations beneath the array, and they

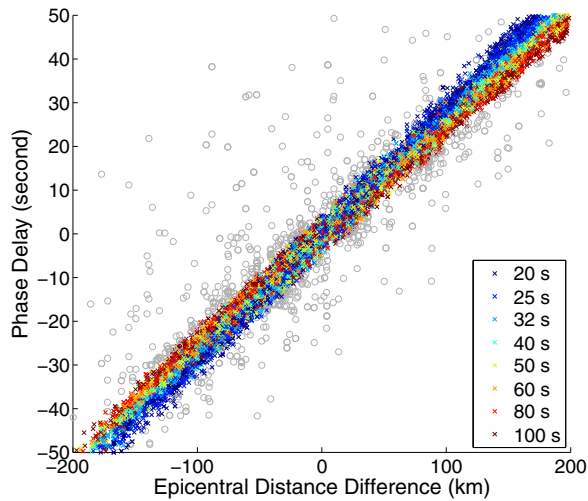


**Figure 4.** Relative phase delays versus epicentral distance difference for all the station pairs with inter-station distance smaller than 200 km, for the Kermadec Islands earthquake. Crosses with different colour represent the measurements at different frequencies, and grey circles represent the poor measurements that are discarded as described in Section 3.2.

form the basis for inverting for phase-velocity variations across the array.

## 2.2 Derivation of apparent phase velocity

For each earthquake and at each frequency, the apparent phase velocity of the wavefield across the array is defined by the Eikonal equation

$$\frac{1}{c'(\vec{r})} = |\nabla \tau(\vec{r})|, \quad (7)$$

where  $\tau(\vec{r})$  is the phase traveltime. Also called the dynamic phase velocity,  $c'(\vec{r})$  is the reciprocal of the traveltime surface gradient, which is close to the structural phase velocity, but will likely be distorted by propagation effects, such as multipathing, backscattering and focusing of the wavefront (Lin *et al.* 2009).

The 2-D networks of interstation phase delays provides a large and well-distributed data set for estimating the phase gradient via tomographic inversion. Unlike the two-station method, all possible nearby station pairs are measured and used to invert for propagation velocity across the array, with no assumptions made about direction of propagation. We use a slowness-vector field to describe the propagation of surface waves, with the vector length representing the reciprocal of apparent phase velocity and vector direction representing the wave-propagation direction (Fig. 5). The phase-delay time between two nearby stations  $\delta\tau_p$  can be described by the integral of the vector field as:

$$\delta\tau_p = \int_{r_i} \vec{S}(\vec{r}) \cdot d\vec{r}, \quad (8)$$

where  $\vec{S}(\vec{r})$  is the slowness vector and  $\vec{r}_i$  is the spherical path connecting the two stations. We invert for the two orthogonal components of the slowness distribution ( $S_R$  and  $S_T$ ) as a function of position across the array.  $S_R$  follows the great-circle path direction from the epicentre, and is positive in most cases.  $S_T$  is orthogonal to  $S_R$  with usually a much smaller value, and can be either positive

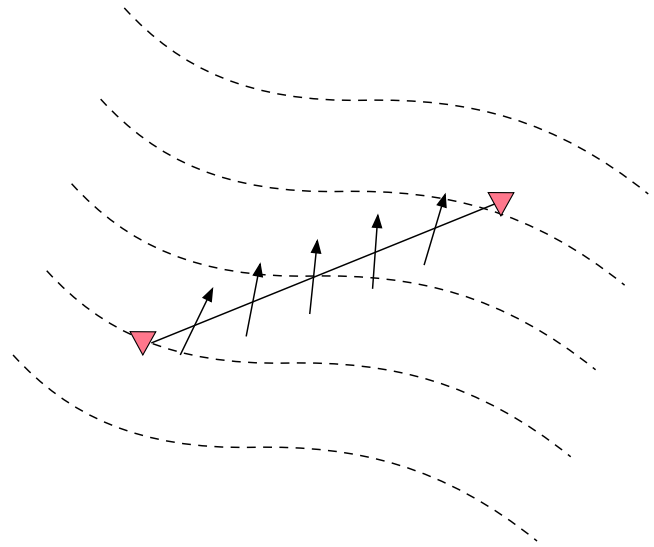


**Figure 5.** Schematic of the slowness-vector inversion. The phase-delay time between any two stations equals to the integral of the slowness vector projected along the link between the stations. Dash lines illustrate wavefronts, red triangles are stations, black line is inter-station link, and black arrows are slowness vectors.

or negative depending on the actual direction of wave propagation. Eq. (8) can also be written in discrete form as:

$$\delta\tau_p = \sum_i (S_{R_i} dr_{R_i} + S_{T_i} dr_{T_i}), \quad (9)$$

where  $dr_{R_i}$  and  $dr_{T_i}$  denote the projections of the  $i$ th segment of the interstation link on the radial and tangential directions, and  $S_{R_i}$  and  $S_{T_i}$  are the radial and tangential components of the slowness vector at location  $i$ .

The inversion is stabilized by using a smoothness constraint that minimizes the second order derivative of  $S_R$  and  $S_T$ . The penalty function being minimized can be presented as:

$$\varepsilon_c^2 = \sum \left| \int_{r_i} \vec{S}(\vec{r}) \cdot d\vec{r} - \delta\tau_{p_i} \right|^2 + \lambda \left( \sum |\nabla^2 S_R|^2 + \sum |\nabla^2 S_T|^2 \right), \quad (10)$$

where the first term is the misfit between observed and predicted phase delay, and  $\lambda$  is a factor to control the smoothness. The left-hand panels of Fig. 7 presents the apparent (Eikonal) phase velocities determined from the  $\delta\tau_p$  data presented in Fig. 4, with the station-pair links used in the inversion shown in Fig. 6. Here, the phase velocities are inverted on a  $0.3^\circ \times 0.3^\circ$  grid. We select the weight  $\lambda$  of the smoothing kernel in the slowness inversion based on the estimation of average signal-to-noise ratio (SNR) and wavelength, which varies at each frequency.

## 2.3 Derivation of structural phase velocity

The bias between apparent phase velocity and structural phase velocity can be corrected by adding amplitude measurements into the inversion, using an approximation to the Helmholtz equation (Wielandt 1993; Lin & Ritzwoller 2011):

$$\frac{1}{c(\vec{r})^2} = \frac{1}{c'(\vec{r})^2} - \frac{\nabla^2 A(\vec{r})}{A(\vec{r})\omega^2}. \quad (11)$$

Here,  $c(\vec{r})$  is the structural phase velocity and  $A(\vec{r})$  is the amplitude field. The amplitude Laplacian term corrects for the influence of

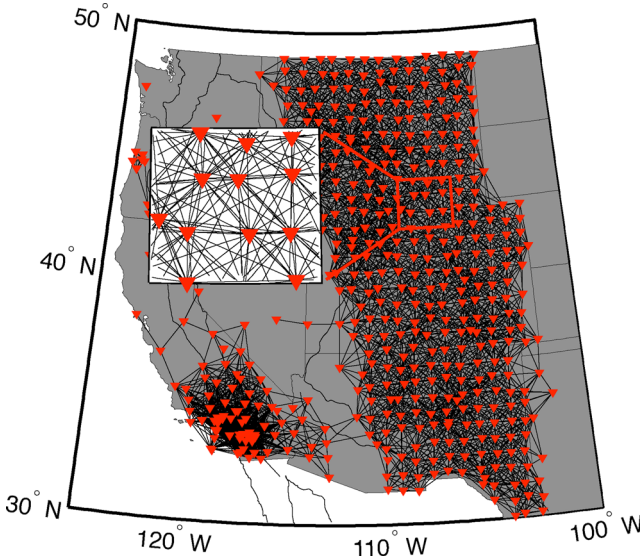


**Figure 6.** Inter-station connections of the slowness-vector inversion for the Kermadec Islands event. Red triangles are station locations and black straight lines are inter-station links, that represent the station pairs with cross-correlation phase delays.

non-plane wave propagation on the apparent phase velocities, allowing for the recovery of the true structural phase velocity (Fig. 7). Lin & Ritzwoller (2011) applied this formulation to USArray data to explore the seismic structure of the western US.

The associated amplitude of the surface wavefield is estimated using amplitude measurements performed on single-station waveforms. As we have applied the five-parameter wavelet fitting to the

windowed and narrow-band filtered autocorrelation function  $\tilde{C}(t)$  to remove the windowing effect in Section 2.1, the scale factor  $\tilde{A}$  of the wavelet is a good approximation of the power spectral density function at the centre frequency of the narrow-band filter.

The input apparent phase velocity  $c'(\vec{r})$  is derived as in Section 2.2 (Figs 7a and e). For the amplitude term, we follow Lin & Ritzwoller (2011) by fitting a minimum curvature surface to the single-station amplitude estimations (Figs 7c and g). The error function for the surface fitting is

$$\varepsilon_A^2 = \sum_i |A(r_i) - A_i|^2 + \gamma \sum_i |\nabla^2 A(\vec{r})|^2, \quad (12)$$

where  $A_i$  is the observed station amplitude at location  $r_i$ ,  $A(r_i)$  is the interpolated amplitude estimated at  $r_i$ , and  $\gamma$  controls the smoothness of the surface. In practice, calculating the second gradients of this amplitude field  $A(\vec{r})$  is sometimes problematic, as the Laplacian operator magnifies short-wavelength noise, and individual amplitude measurements can be highly variable due to local site conditions and erroneous instrument responses. We utilize a finite-difference calculation to estimate the second derivative numerically, and then one more step of smoothing is performed on the correction term to suppress the short-wavelength noise (see Section 5.2 for more details).

The application of the Helmholtz equation implies a consistency between the dynamic phase-velocity and amplitude, which is demonstrated in the right panels of Fig. 7. In particular, wavefield focusing should produce amplitude variations that are consistent with variations in propagation direction. For the example events shown here, local propagation directions estimated from the apparent phase gradients deviate from the predicted great circle path by up to  $\pm 15$  degrees. The regions of wavefield

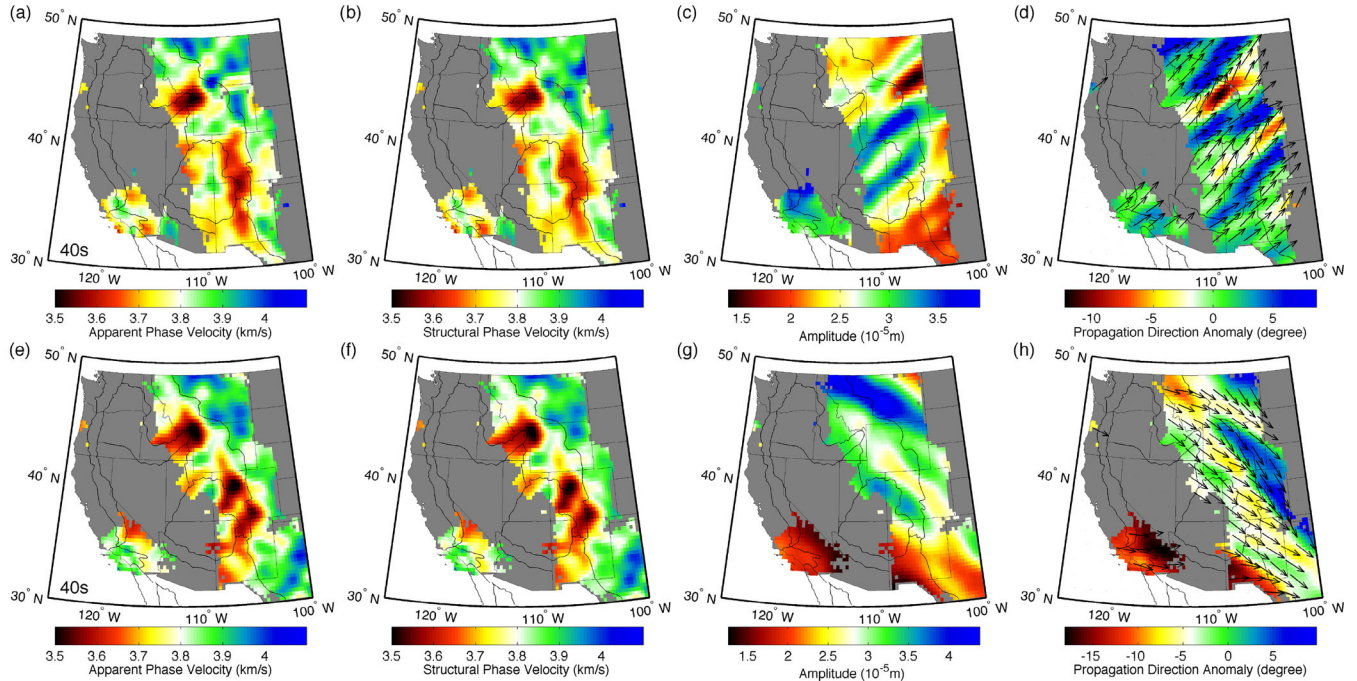


**Figure 7.** The 40-s Rayleigh-wave results of two different events. (a) The apparent phase-velocity map derived from phase-delay measurements (Fig. 4) for the Kermadec Islands event. (b) The corrected phase-velocity map derived from the apparent phase velocity and amplitude measurements via Helmholtz equation. (c) The amplitude map. (d) The map of the propagation direction anomalies. Arrows depict the propagation direction while the colours illustrate the angular difference from the great-circle direction. The rotation of the arrows from great-circle direction is exaggerated for demonstration. (e)–(h) Same as (a)–(d) but for the 2009 April 7, earthquake near Kuril Islands ( $M_s = 6.8$ ).

convergence produced high amplitudes as observed in the data, and low amplitudes correspond to regions of wavefield convergence. The spatial correlation of these independent observations provide confidence for application of the Helmholtz correction.

The amplitude correction cannot be simply applied on Love-wave measurements, as the phase and amplitude measurements of Love waves are made on the tangential component based on the great-circle path direction, which is not necessarily the actual particle-motion direction of the propagating Love-wave field. The presence of multipathing wave fields with conflicting polarizations makes the Helmholtz equation invalid. As a result, all the Love wave results discussed in this paper are the results of Eikonal tomography.

In the following section, we present the full application of this analysis to the data from the TA. The analysis up through the calculation of structural phase velocity is done for individual events, at a range of frequencies. For a fixed array geometry, the resulting phase-velocity maps from individual events are averaged (stacked) to produce the final phase-velocity maps that can be used in a structural inversion for shear velocity. In the case of a rolling array such as the TA, stacking and averaging over multiple events produces a single comprehensive phase-velocity map that spans the history of the array deployment.

### 3 DATA PROCESSING AND AUTOMATION

We apply this analysis to the data collected by USArray from January, 2006 to August, 2014. We collect all events with  $M_w$  larger than 6.0 and depth shallower than 50 km using the software SOD (Owens *et al.* 2004). The station locations and event azimuthal distribution are shown in Fig. 8. Seismograms are pre-filtered from 0.005 to 0.1 Hz, with instrument response deconvolved to displacement. In total about one-half million seismograms from 850 events are processed, generating about four million cross-correlation measurements. This volume of data requires an automated process. Effective automation requires two additional components to the analysis: the generation of the time window to be analysed, and a means to evaluate errors and remove outliers.

#### 3.1 Autogeneration of isolation filter

As the first step of the process, a window function  $W_S$  is required to isolate the fundamental-mode energy of the surface waves. The desired window function  $W_S$  should be wide enough to include the arrivals of the maximum amplitudes of all frequencies, and narrow enough to eliminate the interference from higher mode phases and body waves.

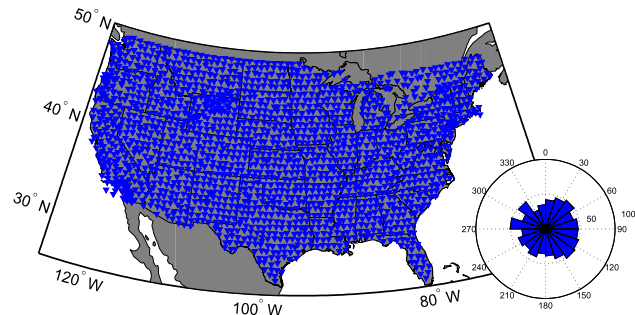


**Figure 8.** Station locations and event azimuthal distribution (insert) from 2006 to 2014.

To generate this window function, we first estimate the group delays of all the frequency bands at individual stations using the frequency-time analysis (FTAN) method (Levshin *et al.* 1992). The desired time-range to be included for each frequency is two cycles before and five cycles after the group delay. At each station, we select the first beginning and last ending time among these time-ranges of all the frequency bands, and define them as the beginning and ending time of the suggested window function of the station.

We collect the locations of suggested window functions for the entire array, and solve for a linear relation between the time range of the final window function  $W_S$  and epicentral distance. The relation is defined as:

$$T_1 = \frac{L}{v_1} + t_1 \quad T_2 = \frac{L}{v_2} + t_2, \quad (13)$$

where  $T_1$  and  $T_2$  are the beginning and ending time of  $W_S$ ,  $L$  is the epicentral distance, and  $v_1, v_2, t_1, t_2$  are the parameters estimated by linear regression.

An example of this automated window selection is shown in Fig. 1. Alternative window selection algorithms include the use of regional/global group-velocity maps in frequency band of interest, or group-velocity predictions using a regionally appropriate 1-D model.

#### 3.2 Autoselection of high-quality measurements

We use the coherence between the waveforms of nearby stations as the primary factor to eliminate measurements with low SNR or from dysfunctional stations. The coherence is frequency dependent and can be estimated by comparing the amplitude of cross-correlation function  $C(t)$  and two autocorrelation functions  $\tilde{C}(t)$ . Since we already fit the five-parameter wavelet to those functions, it is convenient to use those fitting results. Coherence at a certain frequency can be written as:

$$\gamma^2 = \frac{A_{12}^2}{\tilde{A}_{11}\tilde{A}_{22}}, \quad (14)$$

where  $A_{12}$  is the amplitude of the narrow-band cross-correlation wavelet estimated in Section 2.1, and  $\tilde{A}_{11}$  and  $\tilde{A}_{22}$  are the amplitudes of the narrow-band autocorrelation wavelet of the two stations estimated in Section 2.3. In this study, we exclude all the measurements with the coherence lower than 0.5.

The second round of data selection is performed after the phase-delay measurements from all the station pairs are gathered. We estimate the average phase velocity at each frequency by linearly fitting the phase delays with respect to the difference in epicentral distance, and discard all measurements with misfit more than 10 s relative to the linear prediction. For station pairs less than 200 km apart, this is a weak constraint, removing only those observations with traveltime deviations greater than 20 per cent of the total traveltime. For an example event in Fig. 4, this treatment discards 1784 of 41 544 total observations for this event, effectively removing most of the extreme measurements and thus stabilizing the Eikonal inversion.

Following the Eikonal inversion described in Section 2.2, we reject the measurements with large inversion misfit, which is defined as the difference between the predicted and observed phase delay, and invert for the slowness again. This step removes the inconsistent measurements and enhance the robustness of apparent phase velocity results.

For the amplitude measurements, we discard the stations with amplitude variation larger than 30 per cent of the median amplitude of their nearby stations (<200 km).

## 4 RESULTS

We convert the structural phase velocity maps from individual events into slowness, and then they are weighted and stacked. The weighting of each pixel for each event is based on the ray density in the slowness inversion (Section 2.2), and pixels in an individual event map that differ from the stack value by more than two standard deviations are removed. Event maps are utilized only if the number of high-quality, qualified observations exceed a minimum threshold, and we discard events with mean phase velocity that differs by more than 2 per cent of the existing stacked result for the same region. Only the pixels averaging more than 10 events are shown in the maps. After stacking, the phase-velocity maps are further

smoothed, with the smoothing length being a quarter of the average wavelength at each frequency. We focus here on the Rayleigh-wave observations; we also calculate maps for Love waves, but they are not shown, pending further analysis of apparent higher mode contamination.

### 4.1 Phase-velocity variations across the continental US

The Rayleigh-wave phase-velocity maps in eight frequency bands are shown in Fig. 9. Surface waves at a particular frequency are sensitive to the shear velocity structure over a range of depths, thus the phase-velocity anomalies cannot be directly interpreted as the shear-velocity variations at a specific depth. However, higher frequency Rayleigh waves sample shallower structures, with the depth of maximum sensitivity being roughly one-third of the wavelength.

In the western US, large phase-velocity variations outline the major geological structures. Near the Yellowstone hotspot, high

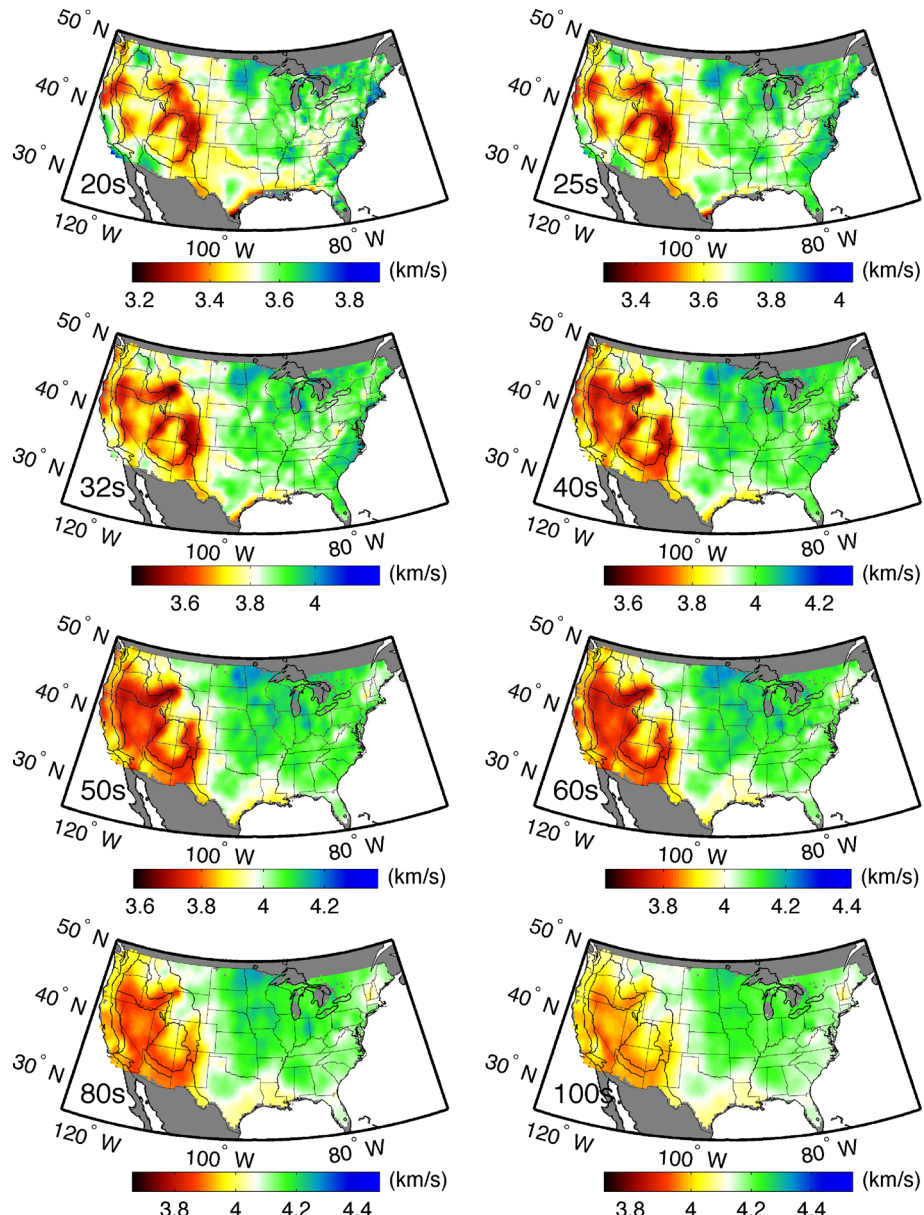


Figure 9. Rayleigh-wave phase-velocity maps at different periods, with 850 events stacked.

temperatures and the possible presence of partial melt are suggested by a strong slow anomaly in all bands. At the adjacent Snake River Plain, the slow anomalies diminish at high frequencies, perhaps due to the faster crustal velocity associated with basaltic volcanism (e.g. Sparlin *et al.* 1982; Peng & Humphreys 1998). At low frequencies, slow anomalies suggest the existence of high temperature source and possible partial melt in the upper mantle (e.g. Saltzer & Humphreys 1997). A similar trend of phase velocity variations (fast at high frequency, slow at low frequency) is observed in the northern Basin and Range, where the crust is thinned due to the Cenozoic extension (e.g. Zandt *et al.* 1995), and the existence of high temperature and partial melt in the upper mantle is suggested by the surface heat flow measurements (e.g. Lysak 1992) and basalt chemistry (e.g. Gazel *et al.* 2012). The deep crustal roots of central and southern Rocky Mountains produce slow anomalies at high frequencies. At low frequencies, as the effect of the thick crust diminishes, the slow anomalies shift to the south, where they are associated with the lithospheric thinning beneath the Rio Grande Rift (e.g. Gao *et al.* 2004). The Colorado Plateau is collocated with relative fast phase velocities compared to the surrounding regions at all frequencies. This is consistent with the reported faster shear velocity in the crust (e.g. Bailey *et al.* 2012), and a thick lithosphere supporting the plateau (e.g. Lee *et al.* 2001). Even at this continental scale, the impingement of low shear velocities into the plateau interior suggests a progressive thermal erosion or destabilization of the edge of the plateau (e.g. Roy *et al.* 2009; Levander *et al.* 2011).

The phase velocities in the eastern US are in general 3–5 per cent higher than those in the western US. However, the magnitudes of the velocity variations are noticeably smaller. At low frequencies, the slow anomaly beneath the New England region suggests thin lithosphere underlain by warmer mantle (e.g. Li *et al.* 2002; Gaherty 2004; Rychert *et al.* 2005). At high frequencies, extremely slow anomalies are observed along the coastline of the Gulf of Mexico, which is attributed to the thick sedimentary layer along the coast (Laske & Masters 1997). The Mid Continent Rift and the Appalachian Highlands are associated with slow anomalies at high frequencies, which probably reflect thickened crust in these two regions (Crotwell & Owens 2005; Parker *et al.* 2013; Shen *et al.* 2013b), while the Northern Atlantic Coastal Plain is colocated with fast anomalies, perhaps indicating thin crust (Crotwell & Owens 2005). Most of these anomalies diminish at periods longer than 40 s, indicating that little thermal variations in the mantle remain associated with these long-lived geologic structures.

In order to better quantify the apparent contrast in the amplitude of the phase-velocity variations between the tectonically active western US and the stable eastern interior, we apply a 2-D Fourier spectral analysis on the Rayleigh-wave phase-velocity maps. Using an approach similar to Chevrot *et al.* (1998), the Fourier transform is performed on sinusoidal map projections centred at  $(40.5^\circ, -113^\circ)$  and  $(38^\circ, -90^\circ)$  for the western and eastern US, respectively (Fig. 10a). We apply a minimum curvature surface interpolation of phase velocity to fill the empty space, and then subtract the average phase velocity of each area to focus on the velocity variations. The 2-D amplitude spectra are then plotted for each period in both regions for all spatial scales larger than the nominal surface wave wavelengths at that period (Fig. 10b).

The spectra of both western and eastern areas (Fig. 10b) indicate a linear increase in the amplitude of heterogeneity with wavelength, which is consistent with global studies at a larger scale (Chevrot *et al.* 1998; Dziewoński *et al.* 2010). This result also agrees with predicted spectrum of heterogeneities from numerical models of fluid convection (e.g. Batchelor 1959; Antonson & Ott 1991;

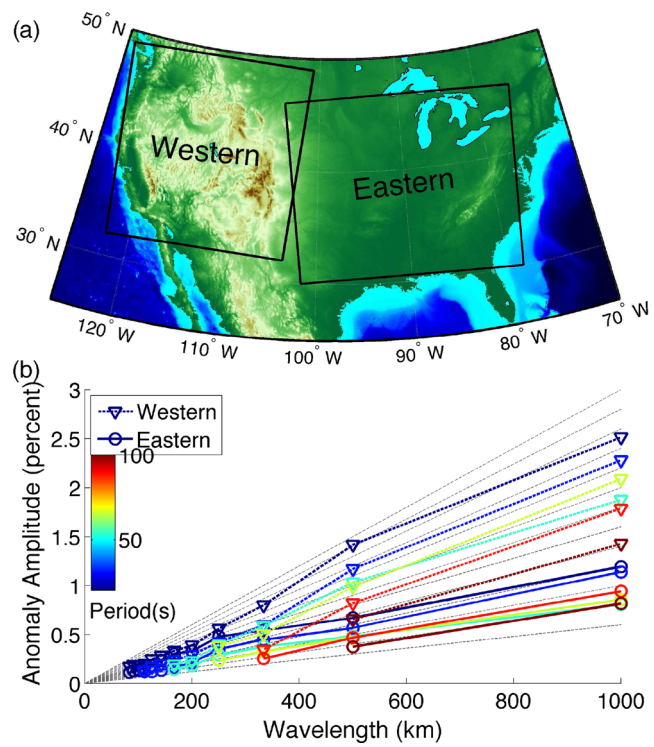


**Figure 10.** 2-D spectral analysis of the Rayleigh-wave phase-velocity maps. (a) The definition of the western and eastern US areas. (b) The amplitude of phase-velocity variations versus the structural wavelength at different periods. Only the structural wavelengths larger than the Rayleigh-wave wavelengths are plotted at each period. The grey dash lines in the background show the predicted  $1/k$  dependence of the heterogeneity strength by thermal convection models (e.g. Ricard *et al.* 2014).

Ricard *et al.* 2014), which suggest that the 1-D power spectrum of the heterogeneities in any direction varies at  $1/k$ , where  $k$  is the wavenumber. This is equivalent to a  $1/k^2$  variation for 2-D power spectrum (Chevrot *et al.* 1998), or  $1/k$  variation for 2-D amplitude spectrum, as what we show in this study.

In the western US, the variation amplitudes measured at the shortest periods (20 and 25 s) are in general much stronger than the variation amplitudes at longer periods. This trend is visible but less obvious in the eastern US. These two frequency bands are highly sensitive to the structure of continental crust, and we interpret this trend as indicating a greater degree of velocity heterogeneity and thickness variation in the crust. Specifically, the velocity heterogeneity likely arises due to the large variation in velocity of common crustal lithologies (e.g. Christensen & Mooney 1995), and the rough topography of Moho in the western US (Shen *et al.* 2013a).

In the eastern US, some Moho depth variations larger than 10 km are reported across various tectonic regions (e.g. Li *et al.* 2002; Parker *et al.* 2013; Shen *et al.* 2013b), but in general they are smaller than those observed in the western US (e.g. Crotwell & Owens 2005; Shen *et al.* 2013a; Levandowski *et al.* 2014). In addition, the density and shear velocity of old orogen crustal roots may increase with greater age due to cooling and metamorphic reaction (Fischer 2002). This would decrease the velocity contrast between the crustal roots and the underlying mantle, and hence reduces the magnitude of phase-velocity variations.

At that periods most sensitive to mantle structure, the variation amplitudes in the western US are 1–2 times greater than those in the eastern US at most spatial wavelengths. These phase-velocity variations are most likely dominated by variations in temperature

(e.g. Priestley & McKenzie 2013; Dalton *et al.* 2014), which are significant in the western US. Ancient orogenic structures in the east (e.g. mid-continent rift system, Grenville Oregon, Piedmont Plateau) likely had large temperature heterogeneity in the past, but thermal diffusion has reduced these variations over time. There is some evidence that at the highest velocity end of the heterogeneity spectrum, compositional structure contributes significantly to observed shear-velocity variations in stable cratonic lithosphere (Dalton *et al.* 2009). It is likely that such structure contributes to the phase-velocity variations observed in the eastern portion of the continent.

## 4.2 Comparison with other studies

### 4.2.1 Comparison with ambient noise results

Microseismic ambient noise has been widely used to retrieve surface wave phase velocity at high frequencies. We compare the highest frequency earthquake phase-velocity results from this study with the ambient noise phase velocities estimated by Ekström (2013). These ambient noise results are also the output of an automated system, which downloads the continuous waveform data, estimates and stacks the normalized coherence, retrieves phase delays between station pairs in the frequency domain (Ekström *et al.* 2009), and produces phase velocity maps using ray theory. The results are regularly updated and can be downloaded from the author's website (<http://www.ledo.columbia.edu/~ekstrom/Projects/ANT/USANT12.html>, last accessed 10 March 2015).

Fig. 11 depicts the comparison for Rayleigh waves and Love waves at a period of 20 s. The results are highly consistent, despite that they are retrieved from different seismic sources by using different phase measurement techniques and velocity inversions. Strong geological features are clearly highlighted in both results.

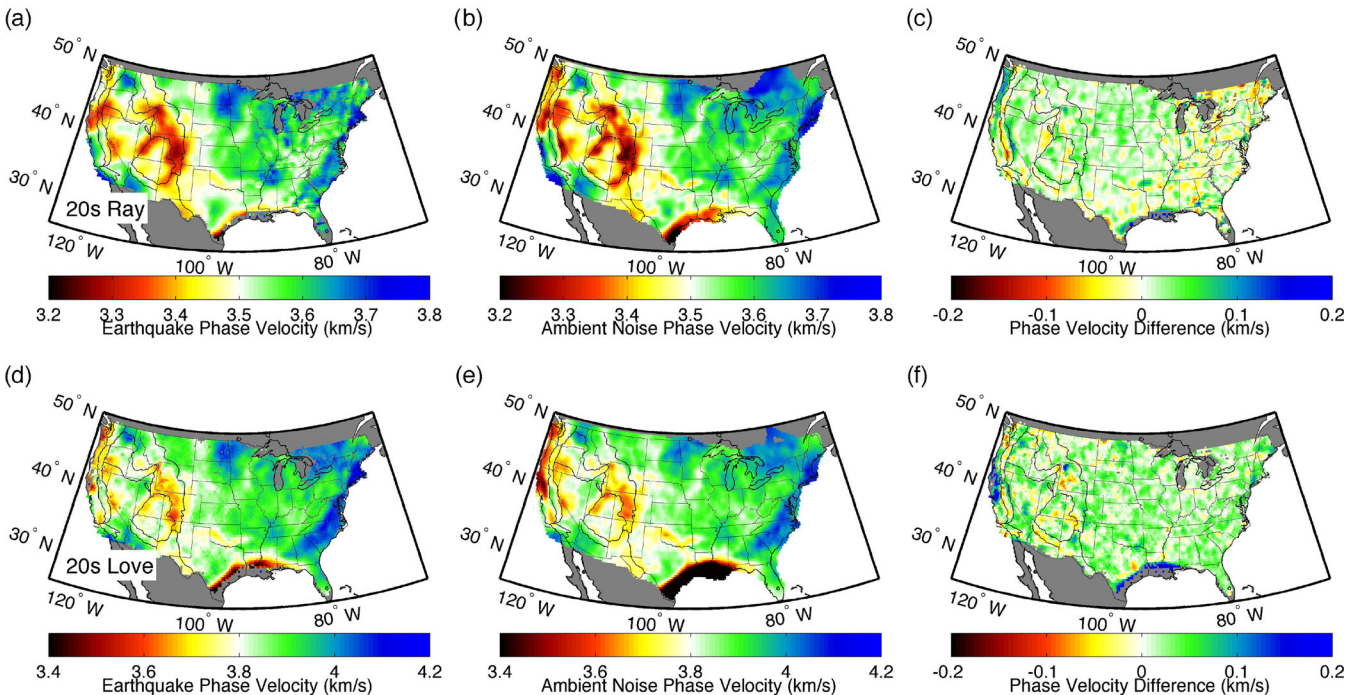


**Figure 11.** Comparison of 20-s Rayleigh and Love wave phase-velocity maps derived from earthquakes (this study) and ambient noise (Ekström 2013). (a) The earthquake result. (b) The ambient noise result. (c) The subtraction of (b) from (a). (d)–(f): Same as (a)–(c), but for Love waves.

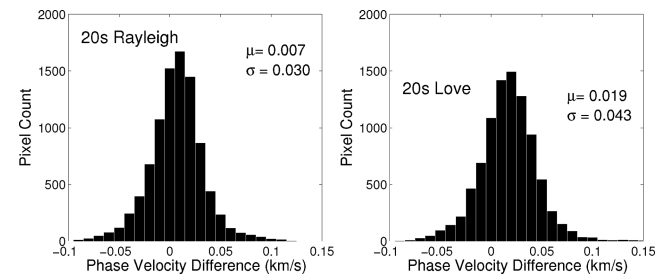


**Figure 12.** Histograms of phase velocity difference between the maps shown in Fig. 11.

The largest inconsistencies (Figs 11c and f) are localized on the edges of the model space, which are the least-well resolved regions in both models. There are also localized differences near major geological boundaries (e.g. the edge of the Sierra Nevada), which may result from different smoothness constraints in the two approaches.

For Rayleigh waves, the correlation coefficient between the two maps in Fig. 11 is 0.95. The mean and the standard deviation of the velocity difference are 0.007 and 0.030 km s<sup>-1</sup>, respectively. The small but systemic difference shows slightly higher velocities (0.2 per cent) from this study (Fig. 12), which we interpret as the influence of the ray-bending effects, as the Helmholtz tomography allows for ray bending while conventional ray theory does not. A similar amount of discrepancy is reported by Lin *et al.* (2009) when comparing the straight-ray and Eikonal tomography results using ambient noise measurements.

The Love wave results are usually less robust because of the higher noise level in the horizontal components. Nevertheless, the correlation coefficient between the two studies is 0.93. The mean and the standard deviation of the velocity difference for Love waves is 0.019 and 0.043 km s<sup>-1</sup>, respectively. The mean difference (0.5 per cent) is almost triple the value of the difference in the Rayleigh wave results.

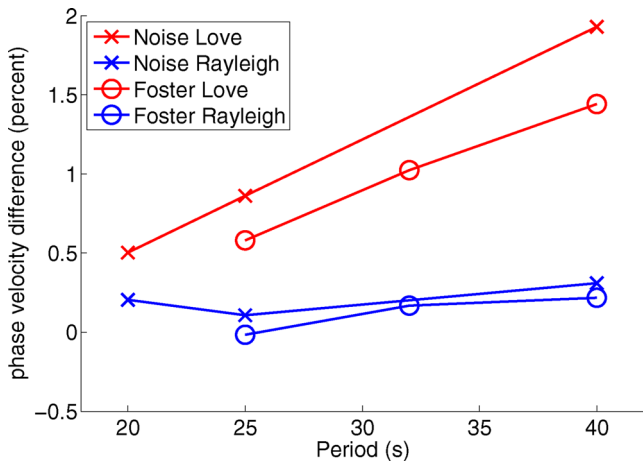


**Figure 13.** The mean phase-velocity difference between this study and the ambient noise results of Ekström (2013) (cross markers) and between this study and the earthquake result of Foster *et al.* (2014a). Rayleigh-wave results show good agreement among the models, while Love-wave results display a systemic bias increasing with period.

We also compare the results at two longer periods (25 and 40 s). The means of the differences are summarized in Fig. 13. For Rayleigh waves, we find the difference between the two studies are small. The correlation coefficients range from 0.971 to 0.982 with slightly increase with period. For Love waves, on the other hand, the systemic bias between the earthquake and the ambient noise measurements increases significantly with period, from 0.5 per cent at 20 s period to 2 per cent at 40 s period. The correlation coefficient drops from 0.925 at 20 s period to 0.888 at 40 s period. We suspect that this bias is mainly controlled by overtone interference, which is discussed in more detail in Section 4.3.3.

#### 4.2.2 Comparison with other earthquake results

We further test our results with comparing them to published phase-velocity maps derived from earthquake-generated surface waves traversing USArray's TA. Lin & Ritzwoller (2011) derive phase-velocity maps for the western US from 40 to 80 s period by applying Helmholtz tomography to single-station phase measurements made using FTAN. Foster *et al.* (2014a) produce phase-velocity maps for the western US spanning 25–100 s period using a modified two-station approach, where the array observations are used to estimate and correct for off-great-circle propagation. In their case the underlying single-station phase measurements are made using Ekström *et al.* (1997).

Figs 13 and 14 present several comparisons between our results and these two models. Fig. 13 summarizes mean velocity difference between our maps and Foster *et al.* (2014a) at 25, 32 and 40 s, across the similar band spanned by Ekström (2013). The Rayleigh-wave results show a high degree of consistency among the studies, with the mean of the difference between them close to zero and correlation coefficient greater than 0.9. The frequency-dependent systematic bias of the Love-wave results indicates the effect of higher-mode interference. This consistency is visually apparent in map form (Fig. 14), and extends to long period. At 60-s period (Figs 14a and b), the comparison with Lin & Ritzwoller (2011) is excellent, with a correlation coefficient between the two maps of 0.97. At 100-s period (Figs 14c and d), the correlation with Foster *et al.* (2014a) is 0.96. Subtle differences in the strength and delineation of individual velocity anomalies are visually apparent

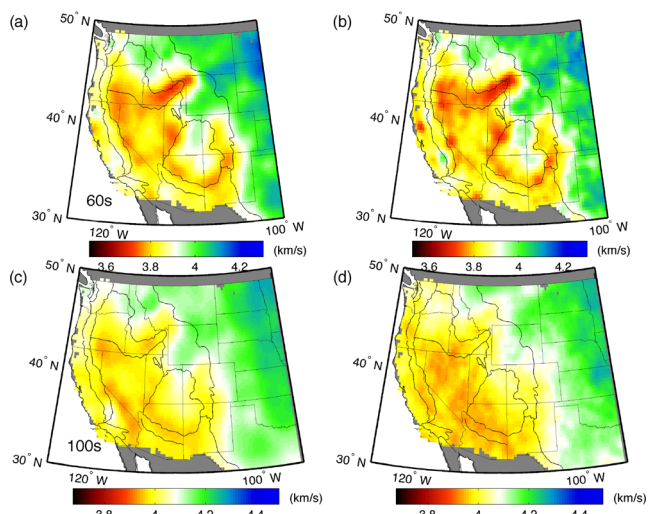


**Figure 14.** Comparison with other earthquake studies at intermediate and long periods. (a) 60-s phase-velocity map from this study. (b) 60-s phase-velocity map from Lin & Ritzwoller (2011). (c) 100-s phase-velocity map from this study. (d) 100-s phase-velocity map from Foster *et al.* (2014a).

between the models, which are likely related to different choices of stacking and smoothing in the modelling. These choices are discussed further in Section 5.

#### 4.3 Possible source of error

##### 4.3.1 Station terms

Although the automated data selection techniques described in Section 3 are able to eliminate most of the poor measurements with low SNR, they are not able to distinguish the stations with a time-shift problem or an abnormal amplification term, as the waveforms of those stations may still correlate well with their neighbors.

A station time-shift can be generated either from clock malfunction or from the incorrect instrument response. If the error is large, the observations can be detected and discarded by the misfit check described in Section 3.2. The stations with smaller timing errors can be distinguished in the apparent phase-velocity maps by the appearance of two short-wavelength anomalies with reversed polarization, located before and after the station in the direction of wave propagation. Those stations can be manually identified and excluded. In general, such errors are not significant in the TA, and we do not perform this manual selection in this study.

The station amplification, on the other hand, is more unavoidable and with less obvious impact compared to the time-shift problem. The amplitude correction we apply in Section 2.3 is based on the assumption that all the stations have the same amplification term, which is not perfect due to variation in local geological structure and installation conditions. The ideal way to eliminate this bias is to first estimate the station amplification by averaging multiple events (Eddy & Ekström 2014), or to invert the phase velocity (include focusing/defocusing terms) and amplification term iteratively Lin *et al.* (2012). However, the amplification term of most stations in the USArray is very close to 1 (Eddy & Ekström 2014), and variation in amplification is generally much smaller and more heterogeneous than the smooth amplitude variations associated with focusing and defocusing. As a result, their influence on the final results of this study is minor.

#### 4.3.2 Azimuthal anisotropy

Lin & Ritzwoller (2011) report the existence of 1–2 per cent of Rayleigh wave azimuthal anisotropy across our frequency range in the western and central US, by using the amplitude correction to further improve the accuracy of the azimuthal-anisotropy estimates. Although this anisotropy almost certainly reflects true structural properties in the crust and upper mantle, accurately estimating anisotropic variations adds significant complexity to the 2-D inversion. Our goal in this study is determine isotropic phase-velocity maps, and we assume that we can ignore anisotropy due to our well-distributed azimuthal distribution of events (Fig. 8). We test this assumption by performing an identical set of phase-velocity inversions, where we include an estimate of azimuthal anisotropy by fitting the structural phase velocity with the wave propagation direction obtained in the slowness inversion. We compare the isotropic part of the azimuthally anisotropic phase velocity models with original isotropic models presented in Fig. 9, and find the difference is smaller than 1 per cent for 95 per cent of the grids, with the median value of 0.4 per cent. These small discrepancies are likely caused by the uneven distribution of source backazimuth in some area, and are negligible in this study.

#### 4.3.3 Overtone interference

We do not observe any significant effects of higher mode interference on the Rayleigh-wave phase-velocity maps, as no significant bias is found between the earthquake and the ambient noise results (Fig. 13). The source of ambient noise is usually believed to be shallow, and therefore the amplitudes of overtones are relatively smaller in the ambient noise waveforms than in the earthquake waveforms. By assuming the ambient noise results being overtone-free, the consistency between the earthquake and the ambient noise result for Rayleigh waves indicates that the effect of overtone interference is small.

For Love waves, the effect of overtone interference on the phase measurement is more significant than for Rayleigh waves, as the difference in the group velocities between the Love-wave fundamental mode and the first few overtones is smaller. We attempt to minimize overtone interference by limiting the analysis to shallow events (<50 km), but the comparison between the earthquake and the ambient noise results still shows a significant frequency-dependent bias (Fig. 13).

In a recent analysis of surface-wave propagation across the TA, Foster *et al.* (2014a) reported a systematically higher phase velocity obtained over short paths from a mini-array velocity analysis (similar to Eikonal tomography) compared to a long-path two-station method (which is shown in Fig. 13). The bias they found for the 50-s Love wave has a similar magnitude to what we observed for the 40-s Love waves. A follow-up study (Foster *et al.* 2014b) suggested that the overtone interference biases phase-velocity estimates derived from local phase-gradient measurements more than those using long ray-path measurements, and the bias generated by this influence can be systematic.

The group velocities of the Love wave fundamental mode and the first mode behave differently in the oceanic and continental structure (Nettles & Dziewoński 2011). In oceanic lithosphere, these two modes propagate at a very similar speed, so it is difficult to distinguish them in the time domain (Gaherty *et al.* 1996). In continents, the group velocity of the fundamental mode drops dramatically at shorter periods (<50 s), whereas the group velocity of the first mode remains high. In general, for the continental stations, the time dif-

ference between the group delays of the fundamental mode and the overtones is largest at higher frequencies, so interference should be minimal there. This interpretation is consistent with the observations that the bias between the earthquake and ambient-noise results increases with period (Fig. 13).

Because the Love wave results are contaminated by overtones interference and hence systematically biased, they are not presented further in this paper. Measuring Love wave phase velocity in the presence of overtone interference will be the subject of a future manuscript.

## 5 DISCUSSION

With the increasing availability of broad-band data from wide-aperture arrays, surface-wave phase-velocity maps are used more than ever for investigating crustal and upper-mantle structure at a variety of scales. Much of the expanded interest has been driven by the development of new analysis techniques that provide robust estimates of structural phase velocity from both ambient noise (e.g. Ekström 2013) and ballistic surface waves, even in the presence of significant multipathing (e.g. Forsyth & Li 2005; Lin & Ritzwoller 2011). These tools have been developed in large part to exploit the capabilities of the latest generation of 2-D arrays, but they are likely leading to an expansion of available array data from around the globe, as more scientists recognize the value of surface waves for regional (e.g. PASSCAL) structural experiments, and they design their arrays accordingly.

The analysis presented here has a number of similarities to established methodologies for estimating phase velocity from earthquake data in the presence of multipathing. Our motivation for pursuing this particular approach is to exploit two strengths of waveform cross-correlation: it provides a highly precise means to estimate velocity within an array, and it can be applied with minimal analyst intervention, making it particularly useful for large data sets such as the USAArray. In developing this method, we explored a number of options for several of the processing steps, including options that are utilized in other techniques, and we present a brief discussion of these issues here.

### 5.1 Comparison to FTAN phase measurement

FTAN method (Levshin *et al.* 1992) is widely used to make phase-and/or group-velocity measurements from single-station surface-wave seismograms in many global or regional surface-wave studies (e.g. Levshin *et al.* 1992; Levshin & Ritzwoller 2001; Lin & Ritzwoller 2011; Yang *et al.* 2011). This method applies a sequences of narrow-band filters to the raw seismograms, and retrieves the group delay at each frequency by tracking the arrival time of the envelope-function maximum. The phase and amplitude measurements are then made at these amplitude maximums for later tomographic inversion. When made at several individual stations within a seismic array, these measurements can be combined to produce interstation phase delays that should be directly comparable to those made via cross-correlation, but in practice they differ in two ways.

First, the two methods exploit different techniques to retrieve phase: this study performs cross-correlation on coherent signals between stations to obtain the relative phase variation, and the FTAN method applies a Hilbert transform to single-station waveforms to retrieve absolute phase values. Cross-correlation can suppress the influence of random noise, which is not coherent among the stations, and therefore provides more robust measurements from

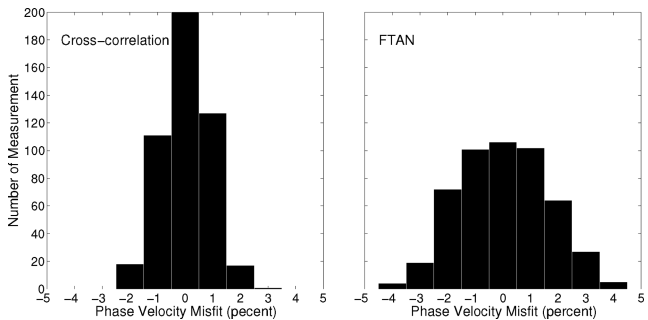


**Figure 15.** Comparison between the cross-correlation measurements and the FTAN measurements in a synthetic test. Left panel: the histogram of the phase-velocity misfit using the cross-correlation method on 500 independent measurements with a 20 per cent noise level. Right panel: the misfit of FTAN measurements of the same data set.

seismograms with relatively low SNR (e.g. Landisman *et al.* 1969). This can be demonstrated by a simple synthetic test, in which a narrow-band wavefield is simulated by a cosine function enveloped by a Gaussian function, propagating with a group velocity of  $3.7 \text{ km s}^{-1}$  and a phase velocity of  $4.0 \text{ km s}^{-1}$ . We add normally distributed random noise to each synthetic wavelet, with a standard deviation of 20 per cent of the wavelet's maximum amplitude. We then measure the phase velocity between 500 station pairs with a station spacing of 50 km along the ray path using both methods. The results (Fig. 15) show that under the same noise level, the standard deviation of the cross-correlation measurements is significantly smaller (50 per cent) than that of the FTAN measurements. In practice, analysts utilizing FTAN can apply SNR criteria to reduce the sensitivity to high random noise levels, but cross-correlation reduces the need for such analyst intervention.

Secondly, the two methods are sensitive to different portions of data. The FTAN method only samples the waveform near the group delay at each frequency, where the surface waves have their largest SNR. At high frequencies, multiple local maxima with similar amplitude may exist within the envelope due to strong scattering (Fig. 16), and selecting inconsistent wavelets across the array may

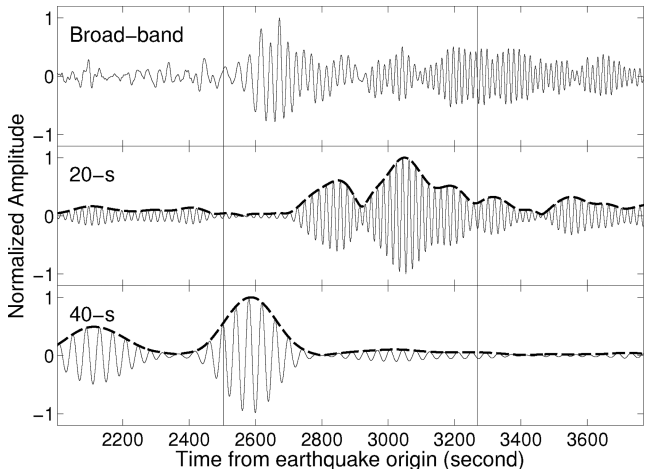


**Figure 16.** Station 327A vertical component record for the same earthquake as in Fig. 1. Top panel: the original waveform filtered from 10 s to 200 s. Middle and bottom panels: the narrow-band filtered waveforms with the centre periods of 20 s and 40 s respectively. The thick dash lines are the envelope functions, two vertical solid lines show the location of the isolation window function  $W_S$ . It is a challenge for the FTAN method to make robust measurements at short periods as the selection of group delay can be uncertain.

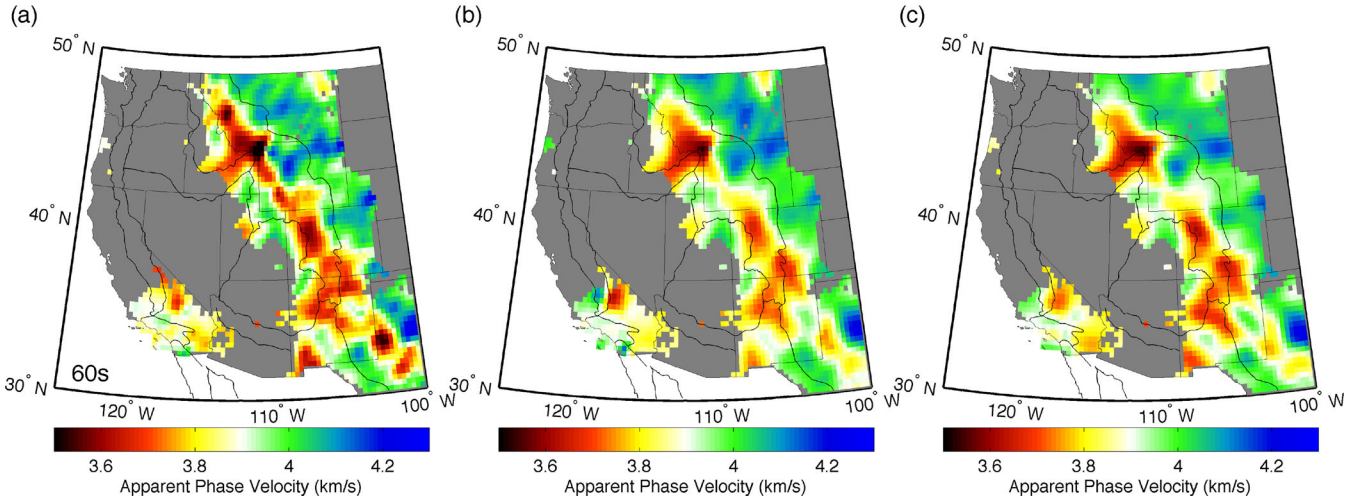
introduce bias into the later phase-velocity inversion. In contrast, the cross-correlation captures the entire surface-wave package, including the coda generated by heterogeneity along the ray path. The phase measurement includes coherent multipathing wavelets, which can be corrected using the amplitude measurements to obtain structural phase velocity. In practice, our method can retrieve robust phase velocities at a period as short as 20 s from teleseismic earthquake data. However, one downside to the cross-correlation algorithm is that the use of a single long broad-band window may result in more significant overtone contamination for Love waves, as discussed in Section 4.3.3.

Fig. 17 compares the two methods using the data of a real earthquake. Fig. 17(a) is the apparent phase-velocity map for a 60 s Rayleigh wave produced using the algorithm described in Lin & Ritzwoller (2011), which corresponds to fig. 4a of their paper. In Fig. 17(b), we replace the FTAN phase measurements with our cross-correlation measurements and keep the velocity inversion the same as Fig. 17(a). The technique to calculate the traveltime surface from multichannel phase-variation measurements can be found in Section 5.3. The comparison between the two plots indicates that our method reduces short-wavelength heterogeneity in apparent phase velocity, most likely due to more stable measurements at low-amplitude stations compared to the FTAN method.

## 5.2 Alternative approaches to Eikonal and Helmholtz tomography

Given a collection of cross-correlation phase delays and station amplitudes, we considered several options in the inversion for both apparent phase velocity (via Eikonal tomography), as well as structural phase velocity (via Helmholtz tomography). Because we measure differential phase between stations instead of absolute phase at individual stations, we directly invert for the orthogonal components  $S_R$  and  $S_\theta$  of the slowness vector, rather than reconstructing the traveltime surface  $\tau(\vec{r})$  and then taking its gradient to obtain apparent phase velocity. This notion provides several advantages. First, we apply the standard slowness-based ray theory as the basis for the inversion, and like conventional ray theory tomography, the ray density serves as a valuable quantification of the data constraints. Directly inverting for the desired variable (slowness and/or phase velocity) provides better control on the smoothness of the inversion, compared to applying smoothing kernels to the integral of slowness (traveltime). For example, minimizing the second derivative of the slowness still allows for it to vary smoothly, whereas minimizing the second derivative of traveltime is comparable to minimizing slowness variation directly. Finally, constraining the smoothness along the radial and tangential directions of the great circle path is more natural for the 2-D propagating wave field than along the latitude and longitude direction. Testing suggests that this approach may not produce significant differences in the apparent phase velocity for the far-field measurements as in this study, but may help the near-field surface fitting for ambient noise studies as in Lin *et al.* (2009).

Figs 17(b) and (c) compares two applications of Eikonal tomography inversion of the same phase measurements. Directly inverting for slowness suppresses high-wavenumber, low-amplitude variations in phase velocity that are likely due to noise, whereas maintaining the magnitude of the stronger, well-resolved anomalies (e.g. the edge of the Colorado Plateau). This improvement has the potential to enhance the resolution of the final structural phase-velocity results, though it is secondary compared to the improvement we



**Figure 17.** 60-s Rayleigh-wave Eikonal tomography results for the April 7, 2009 earthquake near Kuril Islands ( $M_s = 6.8$ ), using different phase-measurement and tomographic-inversions techniques. (a) Phase measurement: FTAN; Tomography: gradient of the traveltime surface. (b) Phase measurement: cross-correlation; Tomography: gradient of the traveltime surface. (c) Phase measurement: cross-correlation; Tomography: slowness vector inversion.

obtain from the cross-correlation phase measurement (Figs 17a and b).

Obtaining the amplitude correction term for Helmholtz tomography presents several challenges. Amplitude measurements are not as robust as phase measurements, as they are susceptible to variations in local amplification and station terms (Lin *et al.* 2012; Eddy & Ekström 2014). Moreover, the correction term relies on the estimation of the amplitude Laplacian. Using finite difference to calculate the second-order derivative of a surface at a certain location requires 9–16 adjacent data points, which is triple that required to estimate the gradient. For the USArray with  $\sim 70$ -km station spacing, the amplitude correction term has a maximum resolution of  $\sim 140$  km (Lin & Ritzwoller 2011). Finally, fitting an amplitude surface by minimizing its curvature does not guarantee the smoothness of its Laplacian term, as shown in Fig. 18(b). Adding fourth order derivative minimization into the damping kernel to fit the amplitude surface was attempted, but no significant improvement was observed.

To partially resolve these difficulties, we adopt a slight modification to the approach of Lin & Ritzwoller (2011). After retrieving the amplitude surface (Fig. 18a) and calculating the second derivative, a rough correction term is generated (Fig. 18b). We then fit a

minimum curvature surface again over this preliminary correction term, with a much larger damping factor to remove any variance with the wavelength shorter than the theoretical resolution (140 km for USArray), as shown in Fig. 18(c). The smoothed correction term can then be applied to clean up the apparent phase velocity map. By comparing Figs 18(d) and 17(c), we can see that the bias generated by multipathing interference is significantly reduced and the shapes of the anomalies are more consistent with the geological structures.

### 5.3 Compatibility with the two-plane-wave method

The two-plane-wave method (TPWM, Forsyth & Li 2005) is widely applied in the field of surface wave tomography. The assumption that the surface wavefield can be approximated by two interfering plane waves can be limiting, in particular for very large arrays, such as the USArray, but the approach has some advantages for small arrays and arrays with irregular station spacing. In its traditional formulation, the TWPM requires significant manual interaction, with amplitude and phase information being measured at individual stations via Fourier analysis, and requiring low-quality data to be manually discarded prior to inversion for phase velocity. In this section, we provide a simple algorithm to convert the

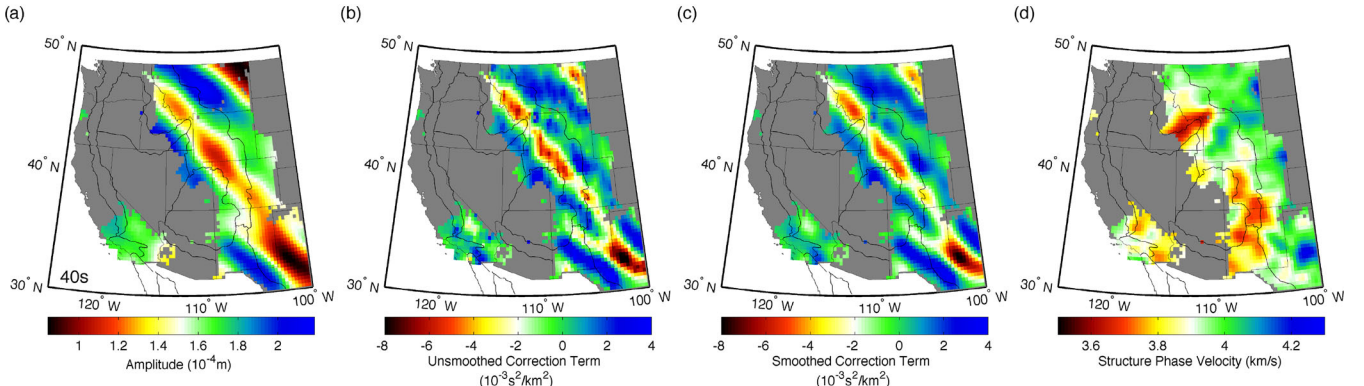


**Figure 18.** Demonstration of the amplitude-correction procedure on the apparent phase-velocity map in Fig. 17(c). (a) The amplitude map generated from the minimum-curvature surface interpolation. (b) The preliminary correction term derived from (a) via Helmholtz equation. (c) The smoothed correction term. (d) The corrected phase velocity map, derived from (c) and Fig. 17(c).

cross-correlation measurements into a format that can be used as the input into the TPWM inversion algorithm.

The TPWM requires the relative phase delays of all stations compared to a reference station. The cross-correlation measurements provide differential phase between station pairs. Each phase difference measurement can be written as

$$\tau_i - \tau_j = \delta\tau_{ij}, \quad (15)$$

where  $\tau_i$  and  $\tau_j$  represent the absolute phases at station i and station j, and  $\delta\tau_{ij}$  is the cross-correlation phase difference measurement derived in this study. To solve for  $\tau_i$ , a matrix formula  $A\tau = \delta\tau$  is built as:

$$\begin{pmatrix} 1 & -1 & 0 & \cdots \\ 1 & 0 & -1 & \cdots \\ 0 & 1 & -1 & \cdots \\ \vdots & \vdots & \vdots & \vdots \end{pmatrix} \begin{pmatrix} \tau_1 \\ \tau_2 \\ \tau_3 \\ \vdots \end{pmatrix} = \begin{pmatrix} \delta\tau_{12} \\ \delta\tau_{13} \\ \delta\tau_{23} \\ \vdots \end{pmatrix}. \quad (16)$$

Where the matrix  $A$  on the left-hand side is redundant but not full rank, as no absolute phase information of any station is given. At this point we need to add one more equation to the set:

$$\tau_1 = 0, \quad (17)$$

by assuming the first station (any station in the array) has zero phase. Then the matrix  $A$  is invertible, and the problem can be solved by a simple least-squares inversion:

$$\tau = (A^T A)^{-1} A^T \delta\tau, \quad (18)$$

where  $\tau$  is now the relative phase delay of all the stations compared to the reference station.  $\tau$  and the array amplitude measurements (Section 2.3) can then be used as the input for TPWM inversion.

## 6 CONCLUSION

We present a new method to measure the surface-wave phase velocity across a seismic array. This method is based on the cross-correlation of waveforms from nearby stations to obtain the phase variations between station pairs. We find that the cross-correlation measurement is more robust than the conventional single-station FTAN measurement under the influence of random noise.

The phase variation and amplitude measurements are inverted for the structural phase velocity using the Helmholtz equation (Lin & Ritzwoller 2011). With the coherence and other data quality estimations serving as selection criteria, we build an automated system that retrieves phase velocity maps directly from seismic data without manual interaction. We apply this system to the USArray TA and produce robust and up-to-date phase velocity maps for the continental US for Rayleigh waves in the 20–100 s band. The Love-wave phase-velocity results are also calculated, but they display systematic bias compared to ambient noise and other results that we interpret as overtone interference. Further study is underway to investigate this phenomenon.

The Rayleigh wave phase velocity maps clearly outline major geological structures (e.g. Snake River Plain, Basin and Range, Colorado Plateau, Yellowstone hotspot, Rocky Mountains, Mid-Continent Rift, Appalachian Mountains), indicating shear velocity variations in the crust and the upper mantle associated with these structures. A 2-D spectral analysis of the phase-velocity maps suggests that the magnitude of velocity variation linearly depends on the structural wavelength. The phase velocity variations in the west-

ern US are on average 1–2 times greater than those in the eastern US at most of the structural wavelengths.

The methodology and automated system we develop in this paper has been adopted by IRIS as a data product to provide weekly updated phase velocity maps of continental US at: <http://www.iris.edu/ds/products/aswms/> (last accessed 10 March 2015). The Matlab code of the Automated Surface-Wave Measuring System (ASWMS) is available at: <https://github.com/jinwar/matgsdf> (last accessed 10 March 2015).

## ACKNOWLEDGEMENTS

The authors thank Colleen Dalton and four anonymous reviewers for their helpful comments that improved the manuscript. We thank Fan-Chi Lin for providing FTAN measurements for comparison, and Anna Foster, Jiayi Xie and Göran Ekström for informative discussion. Weisen Shen provided geological boundaries of the western US and additional FTAN measurements. We are grateful to everyone involved in the deployment and operation of the USArray Transportable Array. Seismic data were collected from the IRIS Data Management Center ([www.iris.edu](http://www.iris.edu)). This research was supported by grants from the National Science Foundation's EarthScope program (EAR-0545777 and EAR-1252039).

## REFERENCES

- Antonsen, T. & Ott, E., 1991. Multifractal power spectra of passive scalars convected by chaotic fluid flows, *Phys. Rev. A*, **44**(2), 851–857.
- Bailey, I.W., Miller, M.S., Liu, K. & Levander, A., 2012. VS and density structure beneath the Colorado Plateau constrained by gravity anomalies and joint inversions of receiver function and phase velocity data, *J. geophys. Res.: Solid Earth*, **117**(B2), B02313, doi:10.1029/2011JB008522.
- Batchelor, G.K., 1959. Small-scale variation of convected quantities like temperature in turbulent fluid Part 1. General discussion and the case of small conductivity, *J. Fluid Mech.*, **5**(01), 113–133.
- Brisbourne, A.M. & Stuart, G.W., 1998. Shear-wave velocity structure beneath North Island, New Zealand, from Rayleigh-wave interstation phase velocities, *Geophys. J. Int.*, **133**(1), 175–184.
- Chen, P., Zhao, L. & Jordan, T.H., 2007. Full 3D tomography for the crustal structure of the los angeles region, *Bull. seism. Soc. Am.*, **97**(4), 1094–1120.
- Chevrot, S., Montagner, J.P. & Snieder, R., 1998. The spectrum of tomographic earth models, *Geophys. J. Int.*, **133**(3), 783–788.
- Christensen, N.I. & Mooney, W.D., 1995. Seismic velocity structure and composition of the continental crust: a global view, *J. geophys. Res.: Solid Earth*, **100**(B6), 9761–9788.
- Crotwell, H.P. & Owens, T.J., 2005. Automated receiver function processing, *Seism. Res. Lett.*, **76**(6), 702–709.
- Dalton, C.A., Ekström, G. & Dziewoński, A.M., 2009. Global seismological shear velocity and attenuation: a comparison with experimental observations, *Earth planet. Sci. Lett.*, **284**(1–2), 65–75.
- Dalton, C.A., Langmuir, C.H. & Gale, A., 2014. Geophysical and geochemical evidence for deep temperature variations beneath mid-ocean ridges, *Science*, **344**(6179), 80–83.
- Dziewoński, A.M., Lekic, V. & Romanowicz, B.A., 2010. Mantle anchor structure: an argument for bottom up tectonics, *Earth planet. Sci. Lett.*, **299**(1–2), 69–79.
- Eddy, C.L. & Ekström, G., 2014. Local amplification of Rayleigh waves in the continental United States observed on the USArray, *Earth planet. Sci. Lett.*, **402**, 50–57.
- Ekström, G., 2013. Love and Rayleigh phase-velocity maps, 5–40 s, of the western and central USA from USArray data, *Earth planet. Sci. Lett.*, **402**, 42–49.

- Ekström, G., Tromp, J. & Larson, E.W.F., 1997. Measurements and global models of surface wave propagation, *J. geophys. Res.: Solid Earth*, **102**(B4), 8137–8157.
- Ekström, G., Abers, G.A. & Webb, S.C., 2009. Determination of surface-wave phase velocities across USArray from noise and Aki's spectral formulation, *Geophys. Res. Lett.*, **36**(18), L18301, doi:10.1029/2009GL039131.
- Fischer, K.M., 2002. Waning buoyancy in the crustal roots of old mountains, *Nature*, **417**, 933–936.
- Forsyth, D.W. & Li, A., 2005. Array analysis of two-dimensional variations in surface wave phase velocity and azimuthal anisotropy in the presence of multipathing interference, in *Seismic Earth Array Analysis of Broad-band Seismograms, AGU Geophysical Monograph Series.*, pp. 81–98, eds Levander, A. & Nolet, G., American Geophysical Union.
- Foster, A., Ekström, G. & Nettles, M., 2014a. Surface wave phase velocities of the Western United States from a two-station method, *Geophys. J. Int.*, **196**(2), 1189–1206.
- Foster, A., Nettles, M. & Ekström, G., 2014b. Overtone interference in array-based love-wave phase measurements, *Bull. seism. Soc. Am.*, **104**(5), 2266–2277.
- Friederich, W. & Wielandt, E., 1995. Interpretation of seismic surface waves in regional networks: joint estimation of wavefield geometry and local phase velocity. Method and numerical tests, *Geophys. J. Int.*, **120**(3), 731–744.
- Gaherty, J.B., 2001. Seismic evidence for hotspot-induced buoyant flow beneath the Reykjanes Ridge, *Science*, **293**(5535), 1645–1647.
- Gaherty, J.B., 2004. A surface wave analysis of seismic anisotropy beneath eastern North America, *Geophys. J. Int.*, **158**(3), 1053–1066.
- Gaherty, J.B. & Dunn, R.A., 2007. Evaluating hot spot-ridge interaction in the Atlantic from regional-scale seismic observations, *Geochem. Geophys. Geosyst.*, **8**(5), doi:10.1029/2006GC001533.
- Gaherty, J.B. & Jordan, T.H., 1995. Lehmann discontinuity as the base of an anisotropic layer beneath continents, *Science*, **268**(5216), 1468–1471.
- Gaherty, J.B., Jordan, T.H. & Gee, L.S., 1996. Seismic structure of the upper mantle in a central Pacific corridor, *J. geophys. Res.*, **101**(B10), 22 291–22 309.
- Gao, W., Grand, S.P., Baldridge, W.S., Wilson, D., West, M., Ni, J.F. & Aster, R., 2004. Upper mantle convection beneath the central Rio Grande rift imaged by P and S wave tomography, *J. geophys. Res.: Solid Earth*, **109**(B3), B03305, doi:10.1029/2003JB002743.
- Gazel, E., Plank, T., Forsyth, D.W., Bendersky, C., Lee, C.T.A. & Hauri, E.H., 2012. Lithosphere versus asthenosphere mantle sources at the Big Pine Volcanic Field, California, *Geochem. Geophys. Geosyst.*, **13**(1), Q0AK06, doi:10.1029/2012GC004060.
- Gee, L.S. & Jordan, T.H., 1992. Generalized seismological data functionals, *Geophys. J. Int.*, **111**(2), 363–390.
- Knopoff, L., Mueller, S. & Pilant, W.L., 1966. Structure of the crust and upper mantle in the Alps from the phase velocity of Rayleigh waves, *Bull. seism. Soc. Am.*, **56**(5), 1009–1044.
- Landisman, M., Dziewoński, A. & Satō, Y., 1969. recent improvements in the analysis of surface wave observations, *Geophys. J. Int.*, **17**(4), 369–403.
- Laske, G. & Masters, G., 1997. A global digital map of sediment thickness, *EOS, Trans. Am. geophys. Un.*, **78**, F483.
- Lee, C.T., Yin, Q., Rudnick, R.L. & Jacobsen, S.B., 2001. Preservation of ancient and fertile lithospheric mantle beneath the southwestern United States, *Nature*, **411**(6833), 69–73.
- Levander, A., Schmandt, B., Miller, M.S., Liu, K., Karlstrom, K.E., Crow, R.S., Lee, C.T. & Humphreys, E.D., 2011. Continuing Colorado plateau uplift by delamination-style convective lithospheric downwelling, *Nature*, **472**(7344), 461–465.
- Levandowski, W., Jones, C.H., Shen, W., Ritzwoller, M.H. & Schulte Pelkum, V., 2014. Origins of topography in the western U.S.: mapping crustal and upper mantle density variations using a uniform seismic velocity model, *J. geophys. Res.: Solid Earth*, **119**(3), 2375–2396.
- Levshin, A., Ratnikova, L. & Berger, J., 1992. Peculiarities of surface-wave propagation across central Eurasia, *Bull. seism. Soc. Am.*, **82**(6), 2464–2493.
- Levshin, A.L. & Ritzwoller, M.H., 2001. Automated detection, extraction, and measurement of regional surface waves, in *Monitoring the Comprehensive Nuclear-Test-Ban Treaty Surface Waves*, pp. 1531–1545, eds Levshin, A.L. & Ritzwoller, M.H., Birkhäuser Basel.
- Li, A., Fischer, K.M., van der Lee, S. & Wysession, M.E., 2002. Crust and upper mantle discontinuity structure beneath eastern North America, *J. geophys. Res.*, **107**(B5), doi:10.1029/2001jb000190.
- Li, X.D. & Romanowicz, B., 1996. Global mantle shear velocity model developed using nonlinear asymptotic coupling theory, *J. geophys. Res.: Solid Earth*, **101**(B10), 22 245–22 272.
- Lin, F.-C. & Ritzwoller, M.H., 2011. Helmholtz surface wave tomography for isotropic and azimuthally anisotropic structure, *Geophys. J. Int.*, **186**(3), 1104–1120.
- Lin, F.-C., Ritzwoller, M.H. & Snieder, R., 2009. Eikonal tomography: surface wave tomography by phase front tracking across a regional broadband seismic array, *Geophys. J. Int.*, **177**(3), 1091–1110.
- Lin, F.-C., Tsai, V.C. & Ritzwoller, M.H., 2012. The local amplification of surface waves: a new observable to constrain elastic velocities, density, and anelastic attenuation, *J. geophys. Res.*, **117**(B6), B06302, doi:10.1029/2012JB009208.
- Lysak, S.V., 1992. Heat flow variations in continental rifts, *Tectonophysics*, **208**(1–3), 309–323.
- Nettles, M. & Dziewoński, A.M., 2011. Effect of higher-mode interference on measurements and models of fundamental-mode surface-wave dispersion, *Bull. seism. Soc. Am.*, **101**(5), 2270–2280.
- Owens, T.J., Crotwell, H.P., Groves, C. & Oliver-Paul, P., 2004. SOD: standing order for data, *Seismol. Res. Lett.*, **75**(4), 515–520.
- Parker, E.H., Hawman, R.B., Fischer, K.M. & Wagner, L.S., 2013. Crustal evolution across the southern Appalachians: initial results from the SESAME broadband array, *Geophys. Res. Lett.*, **40**(15), 3853–3857.
- Peng, X. & Humphreys, E.D., 1998. Crustal velocity structure across the eastern Snake River Plain and the Yellowstone swell, *J. geophys. Res.: Solid Earth*, **103**(B4), 7171–7186.
- Pollitz, F.F. & Snoker, J.A., 2010. Rayleigh-wave phase-velocity maps and three-dimensional shear velocity structure of the western US from local non-plane surface wave tomography, *Geophys. J. Int.*, **180**(3), 1153–1169.
- Priestley, K. & McKenzie, D., 2013. Earth and planetary science letters, *Earth planet. Sci. Lett.*, **381**(C), 78–91.
- Rau, C.J. & Forsyth, D.W., 2011. Melt in the mantle beneath the amagmatic zone, southern Nevada, *Geology*, **39**(10), 975–978.
- Ricard, Y., Durand, S., Montagner, J.P. & Chambat, F., 2014. Is there seismic attenuation in the mantle?, *Earth planet. Sci. Lett.*, **388**(C), 257–264.
- Roy, M., Jordan, T.H. & Pederson, J., 2009. Colorado Plateau magmatism and uplift by warming of heterogeneous lithosphere, *Nature*, **459**(7249), 978–982.
- Rychert, C.A., Fischer, K.M. & Rondenay, S., 2005. A sharp lithosphere–asthenosphere boundary imaged beneath eastern North America, *Nature*, **436**(7050), 542–545.
- Saltzer, R.L. & Humphreys, E.D., 1997. Upper mantle P wave velocity structure of the eastern Snake River Plain and its relationship to geodynamic models of the region, *J. geophys. Res.: Solid Earth*, **102**(B6), 11 829–11 841.
- Schaff, D.P. & Beroza, G.C., 2004. Coseismic and postseismic velocity changes measured by repeating earthquakes, *J. geophys. Res.: Solid Earth*, **109**(B10), B10302, doi:10.1029/2004JB003011.
- Shen, W., Ritzwoller, M.H. & Schulte Pelkum, V., 2013a. A 3-D model of the crust and uppermost mantle beneath the Central and Western US by joint inversion of receiver functions and surface wave dispersion, *J. geophys. Res.: Solid Earth*, **118**(1), 262–276.
- Shen, W., Ritzwoller, M.H. & Schulte Pelkum, V., 2013b. Crustal and uppermost mantle structure in the central U.S. encompassing the Midcontinent Rift, *J. geophys. Res.: Solid Earth*, **118**(8), 4325–4344.
- Sparlin, M.A., Braile, L.W. & Smith, R.B., 1982. Crustal structure of the Eastern Snake River Plain determined from ray trace modeling of seismic refraction data, *J. geophys. Res.: Solid Earth*, **87**(B4), 2619–2633.

- Tape, C., Liu, Q., Maggi, A. & Tromp, J., 2010. Seismic tomography of the southern California crust based on spectral-element and adjoint methods, *Geophys. J. Int.*, **180**(1), 433–462.
- VanDecar, J.C. & Crosson, R.S., 1990. Determination of teleseismic relative phase arrival times using multi-channel cross-correlation and least squares, *Bull. seism. Soc. Am.*, **80**(1), 150–169.
- Wielandt, E., 1993. Propagation and structural interpretation of non-plane waves, *Geophys. J. Int.*, **113**(1), 45–53.
- Yang, Y. & Forsyth, D.W., 2006. Regional tomographic inversion of the amplitude and phase of Rayleigh waves with 2-D sensitivity kernels, *Geophys. J. Int.*, **166**(3), 1148–1160.
- Yang, Y. & Ritzwoller, M.H., 2008. Teleseismic surface wave tomography in the western U.S. using the Transportable Array component of USArray, *Geophys. Res. Lett.*, **35**(4), L04308, doi:10.1029/2007GL032278.
- Yang, Y., Shen, W. & Ritzwoller, M.H., 2011. Surface wave tomography on a large-scale seismic array combining ambient noise and teleseismic earthquake data, *Earthq. Sci.*, **24**(1), 55–64.
- Yao, H., Xu, G., Zhu, L. & Xiao, X., 2005. Mantle structure from inter-station Rayleigh wave dispersion and its tectonic implication in western China and neighboring regions, *Phys. Earth planet. Inter.*, **148**(1), 39–54.
- Zandt, G., Myers, S.C. & Wallace, T.C., 1995. Crust and mantle structure across the Basin and Range–Colorado Plateau boundary at 37°N latitude and implications for Cenozoic extensional mechanism, *J. geophys. Res.: Solid Earth*, **100**(B6), 10 529–10 548.
- Zhu, H., Bozdağ, E., Peter, D. & Tromp, J., 2012. Structure of the European upper mantle revealed by adjoint tomography, *Nat. Geosci.*, **5**(7), 493–498.